molbank

MDPI

Short Note

Methyl 5-(2-Fluoro-4-nitrophenyl)furan-2-carboxylate

Matteo Mori, Andrea Tresoldi, Giulia Cazzaniga, Fiorella Meneghetti * and Stefania Villa

Department of Pharmaceutical Sciences, University of Milan, Via L. Mangiagalli 25, 20133 Milano, Italy
* Correspondence: fiorella.meneghetti@unimi.it

Abstract: 5-Phenyl-furan-2-carboxylic acids have emerged as a new, promising class of antimycobacterial agents that have the ability to interfere with iron homeostasis. Considering the lack of structural data on these compounds, we analyzed the crystal of a fluorinated ester derivative of 5-(4-nitrophenyl)furan-2-carboxylic acid, one of the most potent candidates in the series. Here, we describe the preparation of methyl 5-(2-fluoro-4-nitrophenyl)furan-2-carboxylate (**1**) and its analysis by ^{1}H-NMR, ^{13}C-NMR, HRMS, and SC-XRD.

Keywords: furan; SC-XRD; *Mycobacterium tuberculosis*; antitubercular agent; iron acquisition; MbtI

1. Introduction

Tuberculosis (TB) is currently the second leading cause of death from a single infectious agent after COVID-19 [1]. In 2020, the number of TB deaths increased for the first time in over a decade, mainly due to the health and socio-economic effects of the SARS-CoV-2 pandemic [1]. Moreover, the continuous spread of multi-drug-resistant (MDR) and extensively drug-resistant (XDR) infections has been impacting clinical outcomes in recent years [1]. In this context, the discovery of new drugs that act on unexplored molecular targets represents a necessity as well as a challenge for the scientific community [2]. Over the last decades, a considerable number of compounds, either derived from natural sources or obtained by chemical synthesis, have been investigated as new, potential anti-TB candidates [3–5].

Our research group has devoted much effort to the development of anti-virulence compounds targeting iron acquisition in mycobacteria [6]. In detail, we were able to identify a new class of furan-based inhibitors of the salicylate synthase MbtI from *M. tuberculosis* (*Mtb*) [7]. This enzyme catalyzes the first reaction of the biosynthesis of specific siderophores (mycobactins and carboxymycobactins), which ensure the supply of iron in *Mtb* [8,9]. This metal acts as a cofactor in a variety of processes that allow the establishment and maintenance of the infection in the host [8,9].

Over the years, the scaffold of our furan-based compounds was gradually optimized, leading to promising candidates that are active in mycobacterial models [10–13]. However, high-resolution crystal structures of these compounds are not available in the literature. This is probably due to the fact that 5-phenyl-furan-2-carboxylic acids rarely form high-quality crystals that are suitable for X-ray diffraction analysis. The main reason for such a behavior is their limited solubility in organic and aqueous solvents, which results in their rapid precipitation and prevents the organization of the molecules in an ordered fashion to form a crystal lattice. Therefore, in order to gain preliminary structural information on this class of compounds, we decided to study the more soluble methyl ester derivatives. In detail, we focused our attention on methyl 5-(2-fluoro-4-nitrophenyl)furan-2-carboxylate (**1**), considering that it had shown a propensity to form large, well-shaped crystals in a pre-screening of the available inhibitors. Hence, despite the fact that the corresponding acid only demonstrated modest activity on MbtI [10], this derivative proved to be invaluable for the understanding of the structural features of this class of compounds.

Citation: Mori, M.; Tresoldi, A.; Cazzaniga, G.; Meneghetti, F.; Villa, S. Methyl 5-(2-Fluoro-4-nitrophenyl) furan-2-carboxylate. *Molbank* **2022**, *2022*, M1492. https://doi.org/10.3390/M1492

Academic Editor: Kristof Van Hecke

Received: 18 October 2022
Accepted: 10 November 2022
Published: 12 November 2022

2. Results and Discussion

2.1. Chemistry

Compound **1** was prepared by a modified Meerwein arylation between 2-fluoro-4-nitroaniline and methyl 2-furoate, as previously described (Scheme 1) [10]. The identity of the compound was confirmed by ^{1}H-NMR, ^{13}C-NMR, and HRMS.

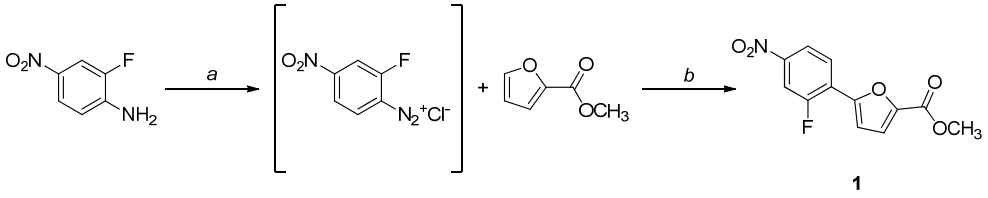

Scheme 1. Synthetic procedure for the preparation of **1**. **Reagents and conditions:** (***a***) $NaNO_2$, conc. HCl, 30 min, 0 °C; (***b***) $CuCl_2$, acetone/water, 3 h, 0 °C → rt.

2.2. Crystallization and Structure Determination

Compound **1** was crystallized from a 1:1 acetone/ethanol solution by slow evaporation; big, well-shaped, orange, prismatic crystals grew within 1—2 weeks at room temperature. After being cut to a suitable size, a sample was analyzed by X-ray diffraction, revealing a monoclinic cell, space group $P2_1/c$. The ORTEP [14] diagram indicating the arbitrary atom-numbering scheme used in the discussion is presented in Figure 1.

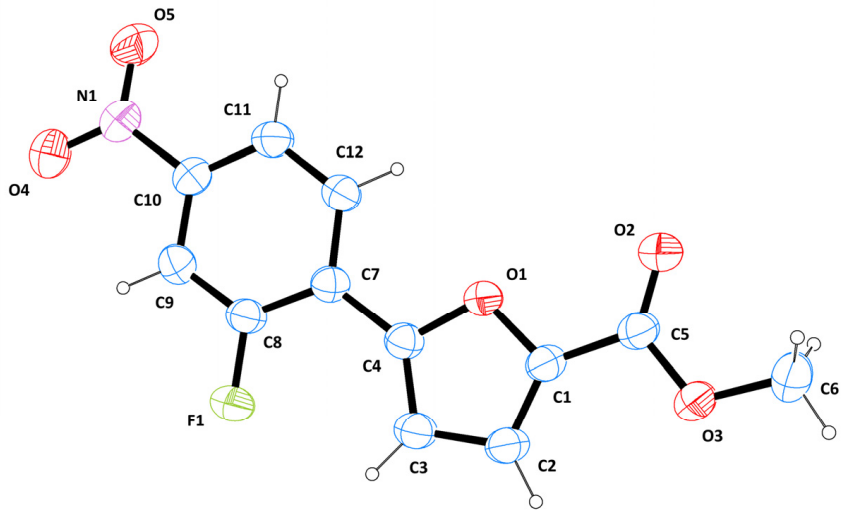

Figure 1. ORTEP diagram of **1**, with the arbitrary atom-numbering scheme. Displacement ellipsoids were drawn at the 40% probability level.

The structure is almost completely planar, with slightly bent sides. The angle between the best mean planes calculated for the furan and the phenyl groups is 3.3(1)°, while the plane formed by C1-C5-O3-C6 is at 3.3(2)° with respect to the furan. The values of the main torsion angles are as follows: C2-C1-C5-O3 = 0.2(2)°; C3-C4-C7-C8 = 1.8(3)°; C9-C10-N1-O4 = 2.9(2)°. All bond lengths, valence angles, and torsional angles are within the expected limits, as shown by CSD Mogul. In detail, bond length values indicate an electron delocalization extending over the entire molecule. The conformation of the molecule, with the fluorine atom oriented towards the "base" of the furan ring, is stabilized by a non-traditional intramolecular CH···F bond between F1 and H3 (H···A = 2.43(1) Å; D···A = 2.87(2) Å; D-H···A = 109.5(1)°). These values are in agreement with the literature [15,16].

The packing is governed by van der Waals interactions between the aromatic rings of adjacent molecules, resulting in a two-dimensional-sheet structure, in which the molecules in the two layers are inclined at an angle of 79.7(1)° (Figure 2). In detail, the phenyl

moieties are involved in stacking interactions, with a centroid–centroid distance of 3.82(4) Å. Moreover, heteroaromatic π-π stacking between the furan and the phenyl rings (centroid–centroid distance of 3.72(1) Å) contributes to stabilizing the structure. Interestingly, H-bonds play only a marginal role in the crystal packing, with just weak C-H···O contacts (Table 1, Figure 2). An additional C-F···O interaction could also be hypothesized between F1 and O3 ($d_{F\cdots O}$ = 3.05(1) Å; ϑ_{CFO} = 161.2(2)°). Overall, we can conclude that the intermolecular contacts do not significantly impact the conformation of the molecule.

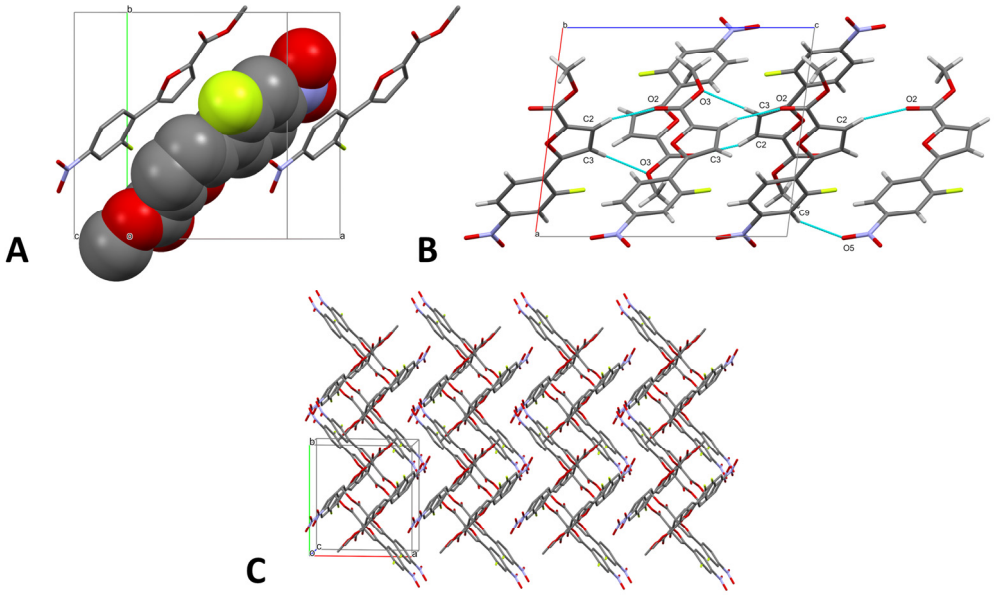

Figure 2. (**A**) Stick-spacefill model of **1** evidencing the stacking interactions between the aromatic moieties of the molecule, viewed along the *c* axis. Hydrogens are omitted for the sake of clarity. (**B**) Stick model of **1** showing the main H-bonds, viewed along the *b* axis. (**C**) Crystal packing of **1**, viewed along the *c* axis. Hydrogens are omitted for the sake of clarity.

Table 1. H-bond geometry (D: Donor, A: Acceptor).

H-Bond	D-H/Å	H···A/Å	D···A/Å	D-H···A/°
C2-H2···O2 ^{I}	0.930(2)	2.622(1)	3.280(2)	128.27(9)
C9-H9···O5 ^{II}	0.930(1)	2.559(1)	3.394(2)	149.57(10)
C3-H3···O3 ^{III}	0.930(2)	2.570(1)	3.496(2)	173.53(10)

Equivalent positions: ^{I} x,$\frac{1}{2}-$y,z+$\frac{1}{2}$; ^{II} x,$-$y-$\frac{1}{2}$,z+$\frac{1}{2}$; ^{III} 1$-$x,y$-\frac{1}{2}$,$^{3}/_{2}-$z.

To further characterize the intermolecular contacts, the Hirshfeld surface of **1** was mapped over the normalized contact distance (d_{norm}), according to the following equation:

$$d_{norm} = \frac{d_i - r_i^{vdW}}{r_i^{vdW}} + \frac{d_e - r_e^{vdW}}{r_e^{vdW}}$$

where d_i is the distance between the HS and the nearest nucleus inside the surface, d_e is the distance between the HS and the nearest nucleus outside the surface, and r^{vdW} represents the van der Waals radius of the atom. Details of the HS are provided in Table 2.

Table 2. Details of the HS generated for **1**.

1	**V (Å^3)**	**A (Å^2)**	***G***	**Ω**
HS	279.75	275.54	0.751	0.372

The d_{norm} property was visualized with a red-blue-white color scheme, which was based on the length of the intermolecular contacts with respect to the sum of the van der Waals radii (Figure 3A) [17]. An analysis of the surface revealed the strong prevalence of blue-white areas and just a few feeble red spots, which correspond to weak H-bonds or random close contacts. The shape index (SI, Figure 3B) property mapped over the HS evidenced a relatively unperturbed structure, which is consistent with the planar character of the molecule. Moreover, the predominance of stacking interactions was confirmed by the typical color pattern of the SI. This observation was confirmed by the curvedness plot (Figure 3C), which evidenced a large planar area extending over the whole molecule on one side and over smaller but still significant planar portions on the other.

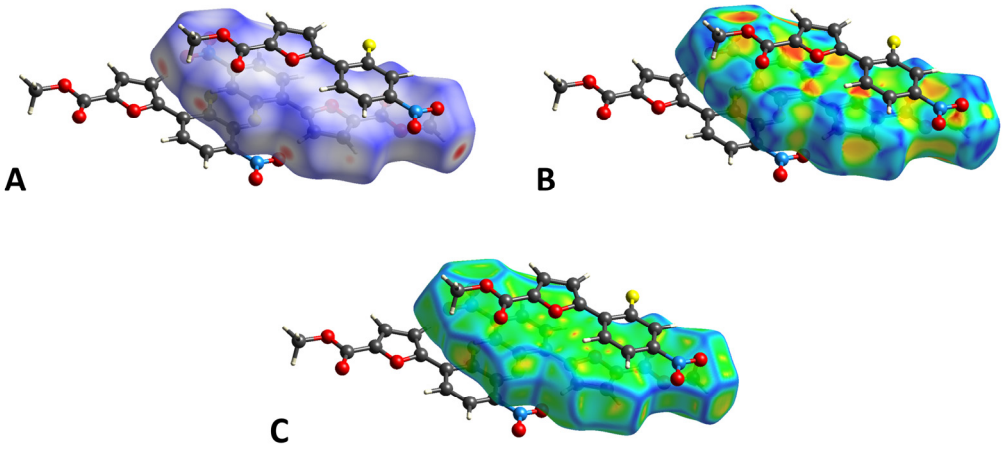

Figure 3. (**A**) HS mapped over d_{norm} with a fixed color scale in the range of −0.1942 au (red)–1.1392 au (blue), based on the length of the intermolecular contacts with respect to the sum of the van der Waals radii (red: shorter; blue: longer; white: same). (**B**) HS mapped over the shape index (color scale: −0.9896 au–0.9973 au). Blue areas represent bumps, and red regions indicate hollows. (**C**) HS mapped over the curvedness (color scale: −3.3180 au–0.2180 au). Flat regions are in green, while edges are in blue.

The two-dimensional (2D) fingerprint of the HS (Figure 4), which provides a visual summary of the contribution of each contact type and the relative area of the surface corresponding to it, is characterized by its compact shape and is highly localized in the upper-right portion of the plot, thus indicating the prevalence of long-range interactions. The largest portion of the HS was constituted by O···H/H···O contacts (38.9%); however, the absence of spikes confirmed the lack of strong H-bonds, indicating the marginal role of these interactions in consolidating the crystal packing. Unspecific van der Waals forces, represented by H···H and C···H/H···C contacts, occupied the next most conspicuous portions of the HS, with 20.3% and 9.1%, respectively. The presence of C···C contacts (8.9%), mainly representing the critical π-π stacking of the aromatic rings, was corroborated by the characteristic arrow-shaped area in the center of the plot. Moreover, the high density of the green spots at 1.8–1.9 Å d_e/d_i confirmed the high contribution of these points on the HS. The remaining contacts are indicated in Figure 4. The calculation of the contact enrichment ratios (Table 3), performed according to Jelsch et al. [18], further substantiated the previous observations. Interestingly, the O···F/F···O contacts proved to be enriched with respect to the corresponding random interactions despite their negligible contributions to the crystal packing.

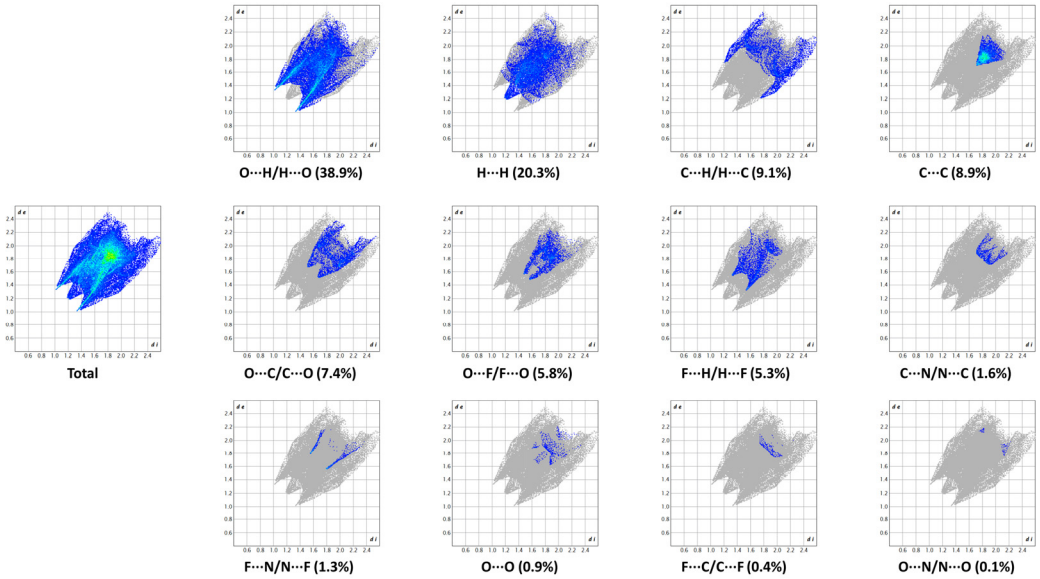

Figure 4. Two-dimensional fingerprint plots of the HS of **1**, providing a visual summary of the frequency of each combination of d_e and d_i across the HS. Points with a contribution to the surface are colored blue for a small contribution, and green for a great contribution.

Table 3. Analysis of the intermolecular contacts on the HS of **1**, according to Jelsch et al. [18]. The first part of the table gives the surface contribution S_X of each chemical type *X* to the Hirshfeld surface. The second part shows the proportions of the actual contacts (C_{XY}), and the third part indicates the enrichment ratios (E_{XY}) of the various contact types. Reciprocal contacts X···Y and Y···X are merged. The E_{XY} were not computed when the random contacts (R_{XY}) were lower than 0.9%. E_{XY} larger than unity indicate enriched contacts (in bold), while those lower than unity are impoverished. The percentages of actual contacts were calculated using CrystalExplorer21.5.

Atoms	**H**	**C**	**N**	**O**	**F**
Surface (%)	47.0	18.2	1.5	27.0	6.4
Contacts (%)					
H	20.3				
C	9.1	8.9			
N	0	1.6	0		
O	38.9	7.4	0.1	0.9	
F	5.3	0.4	1.3	5.8	0
Enrichments					
H	0.9				
C	0.5	**2.7**			
N	0	–	–		
O	**1.5**	0.8	–	0.1	
F	0.9	0.2	–	**1.7**	–

2.3. NMR Analysis and Conformational Study

Fluorine-19 is 100% abundant, has a spin of $\frac{1}{2}$, and its gyromagnetic ratio is similar to that of protons. As a result, H-F and C-F couplings are usually observed in standard ^{1}H and ^{13}C-NMR experiments. These additional heteronuclear interactions determine the complication of the spectra, which can sometimes be difficult to interpret. However, they can also provide insights into the conformation of the molecule. In the present case, the analysis of the NMR spectra suggested that the spatial arrangement of **1** in the solid state was also likely to be the most stable in solution. A first hint was provided by the ^{1}H-NMR (Figure 5A), which showed a coupling between H3 (atom numbering as in Figure 1) and the

fluorine atom, resulting in an apparent triplet instead of the expected doublet. However, it was the ^{13}C-NMR spectrum (Figure 5B) that offered an even clearer indication; in detail, the signal corresponding to C3 was characterized by an unusually large $J_{C\text{-}F}$ coupling (13.1 Hz), considering the number of interconnecting bonds. This has also been observed in similar structures in the literature [19]. Therefore, we inferred that this large value was due to the close interaction of the C3 and F1 atoms through space. A similar conclusion was drawn by Chen and collaborators, who observed a correlation between the detection of a long-range $J_{C\text{-}F}$ coupling and the spatial proximity of the two atoms, as evidenced by SC-XRD studies on a series of BODIPY derivatives [20]. Our hypothesis was further confirmed by geometry optimization studies carried out at the semi-empirical level using MOPAC2016 [21]. The use of different Hamiltonians (AM1, PM3, PM6, PM7, RM1) led to comparable results, which were in agreement with the crystallographic structure. In detail, the C3-F1 distance in the simulated structure was in the range of 2.87–2.98 Å, which was consistent with the distance of 2.87(2) Å observed experimentally.

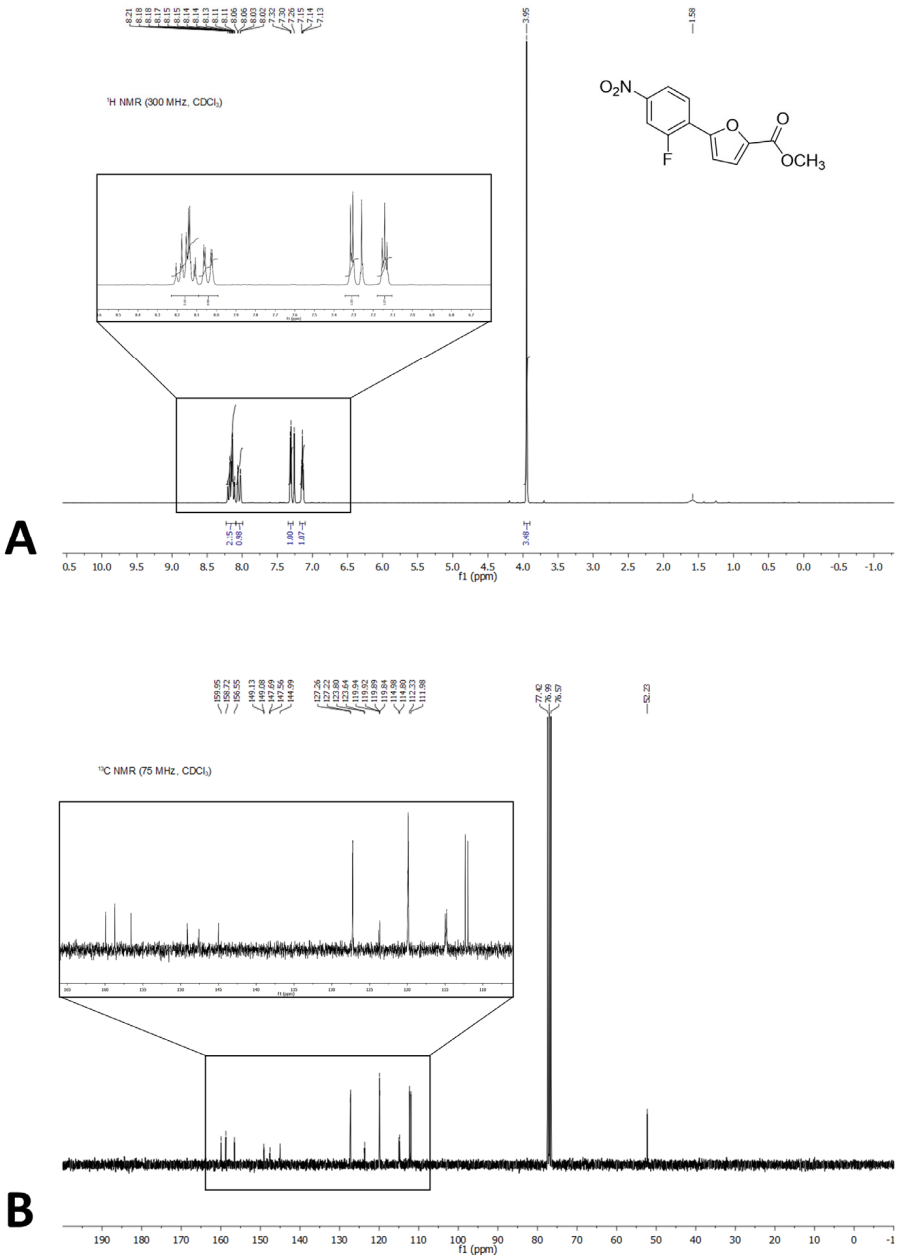

Figure 5. (**A**) ^{1}H-NMR spectrum of **1**. (**B**) ^{13}C-NMR spectrum of **1**.

3. Materials and Methods

3.1. Chemistry

All reagents and solvents were purchased from Sigma-Aldrich (St. Louis, MO, USA). The course of the reaction was followed by thin-layer chromatography (TLC) using aluminum-backed Silica Gel 60 plates (0.2 mm; Merck, Darmstadt, Germany). The crude product was purified by flash column chromatography on silica gel 60 (40–63 μm; Merck, Darmstadt, Germany), using the indicated solvent system. The melting point was determined in an open capillary tube with a Stuart SMP30 Melting Point Apparatus (Cole-Parmer Stuart, Stone, UK). Compound **1** was characterized by means of ^{1}H and ^{13}C-NMR on a Varian Oxford 300 MHz instrument (Varian, Palo Alto, CA, USA), which was operated at 300 MHz for ^{1}H and 75 MHz for ^{13}C (T = 20 °C). The chemical shifts were expressed in ppm (δ), and *J*-couplings were given in Hertz. ^{1}H data were reported in the following order: ppm, multiplicity (s, singlet; d, doublet; t, triplet; q, quartet; m, multiplet), number of protons, and assignment. For the sake of clarity, the arbitrary atom-numbering scheme indicated in Figure 1 was also used to define the signal attributions. The high-resolution mass spectrometry (HRMS) analysis was carried out on a Q-ToF Synapt G2-Si HDMS system (Waters, Milford, MA, USA).

*Methyl 5-(2-fluoro-4-nitrophenyl)furan-2-carboxylate (**1**).* 2-Fluoro-4-nitroaniline (500 mg, 3.2 mmol) was dissolved in 6 M HCl (5 mL), and the solution was cooled to 0 °C in an ice bath. Then, an aqueous solution of $NaNO_2$ (83 mg, 1.2 mmol) was added, keeping the temperature between 0–5 °C. The so-obtained diazonium salt was reacted with a solution of methyl furan-2-carboxylate (378 mg, 3.0 mmol, 320 μL) and $CuCl_2$ (29 mg, 0.214 mmol) in acetone (1.88 mL), which was added dropwise under stirring. During the process, the temperature was maintained in the range of 20–30 °C. After 3 h, the formed precipitate was filtered off and purified by flash column chromatography (cyclohexane–EtOAc 9:1) in order to give the desired product as an orange solid. Yield: 14%. TLC (cyclohexane–EtOAc 8:2): R_f = 0.39. Mp: 196.3 °C. ^{1}H-NMR (300 MHz, $CDCl_3$) δ (ppm): 8.24–8.08 (m, 2H, H9,11), 8.08–7.99 (m, 1H, H12), 7.31 (d, *J* = 3.7 Hz, 1H, H2), 7.14 (t, *J* = 3.7 Hz, 1H, H3), 3.95 (s, 3H, $H6_{A,B,C}$). ^{13}C-NMR (75 MHz, $CDCl_3$) δ (ppm): 158.72 (C5), 158.25 (d, $^{1}J_{C\text{-}F}$ = 256.3 Hz, C8), 149.11 (d, $^{3}J_{C\text{-}F}$ = 3.6 Hz, C4), 147.62 (d, $^{3}J_{C\text{-}F}$ = 9.6 Hz, C10), 144.99 (C1), 127.24 (d, $^{3}J_{C\text{-}F}$ = 3.1 Hz, C12), 123.72 (d, $^{2}J_{C\text{-}F}$ = 12.1 Hz, C7), 119.93 (d, $^{5}J_{C\text{-}F}$ = 1.5 Hz, C2), 119.86 (d, $^{4}J_{C\text{-}F}$ = 3.9 Hz, C11), 114.89 (d, $^{4}J_{C\text{-}F}$ = 13.1 Hz, C3), 112.15 (d, $^{2}J_{C\text{-}F}$ = 26.9 Hz, C9), 52.23 (C6). HRMS (ESI/Q-ToF): *m*/*z* calcd. for $C_{12}H_8NO_5FNa$ 288.0284, found 288.0291.

3.2. X-ray Diffraction

Diffraction data were acquired on an Enraf-Nonius CAD4 four-circle diffractometer (Enraf-Nonius, Delft, Holland), working at ambient temperature with graphite-monochromatized Mo-Kα X-radiation (λ = 0.7107 Å). SC-XRD data were collected using a profiled ω-scan mode, with scan angles of (1.5 + 0.35tanθ)° and a pre-scan speed of 4.12°/min. Accurate unit-cell parameters were obtained by a least-squares fit of the 2θ values for 25 reflections in the 2θ range 14–30°. Data reduction (including intensity integration, background, Lorentz, and polarization corrections) was performed with the WinGX.v2014.1 package [14]. Absorption effects were evaluated by the psi-scan method, and relative correction was applied to the data (min/max transmission factors were 0.796/0.834). The structure was solved by direct methods using SIR-2019 [22] and was completed by iterative cycles of full-matrix least-squares refinement on the F_0^2 and ΔF synthesis; SHELXL-18/3 [23] on the WinGX suite was used [14]. Hydrogen atoms were introduced at calculated positions in their described geometries and were allowed to ride on the attached atom with fixed isotropic thermal parameters (1.2 U_{eq} of the parent atom for aromatic CH groups, 1.5 U_{eq} of the parent atom for the CH_3 group). The structure was analyzed by PARST [24], Mogul [25], and Mercury 2022.2.0 [26]; the graphical representations were rendered with Mercury [26]. HS analysis was performed with CrystalExplorer21.5 [27]. CCDC entry 2213557 contains the supplementary crystallographic data for this paper. A summary of the data collec-

tion and refinement statistics is reported in Table 4; further details are reported in the Supplementary Materials.

Table 4. Summary of the crystallographic data and refinement statistics for **1**.

Parameter	Data	
Identification code	**1**	
Empirical formula	$C_{12}H_8FNO_5$	
Formula weight	265.19	
Temperature	293(2) K	
Wavelength	0.71073 Å	
Crystal system	Monoclinic	
Space group	$P2_1/c$	
Unit cell dimensions	a = 9.6920(10) Å	α = 90°
	b = 10.324(2) Å	β = 97.521(12)°
	c = 11.5182(18) Å	γ = 90°
Volume	1142.6(3) $Å^3$	
Z	4	
Density (calculated)	1.542 Mg/m^3	
Absorption coefficient	0.132 mm^{-1}	
F(000)	544	
Crystal size	0.65 × 0.50 × 0.43 mm^3	
θ range for data collection	2.120 to 30.008°	
Index ranges	$-13 \leq h \leq 13$, $0 \leq k \leq 14$, $0 \leq l \leq 16$	
Reflections collected	3555	
Independent reflections	3333 [$R_{(int)}$ = 0.0064]	
Completeness to θ = 25.242°	100.0%	
Refinement method	Full-matrix least-squares on F^2	
Data/restraints/parameters	3333/0/172	
Goodness-of-fit on F^2	1.077	
Final R indices [I > 2σ(I)]	R1 = 0.0488, wR2 = 0.1221	
R indices (all data)	R1 = 0.0568, wR2 = 0.1327	
Largest diff. peak and hole	0.196 and −0.192 $eÅ^{-3}$	

4. Conclusions

In the framework of our studies on 5-phenylfuran derivatives as antimycobacterial agents, we investigated the three-dimensional structure of methyl 5-(2-fluoro-4-nitrophenyl) furan-2-carboxylate (**1**). This compound was chosen due to its good solubility and propensity to form high-quality crystals. Therefore, **1** was synthesized and characterized by NMR spectroscopy, HRMS spectrometry, and SC-XRD. An analysis of the crystal structure revealed the prevalence of stacking interactions, with only a marginal contribution from long-range CH···O bonds. Overall, the intermolecular contacts did not significantly impact the conformation of the molecule. The NMR experiments and geometry optimization strategies indicated that the conformation of the crystallographic structure was also the most stable in solution.

Supplementary Materials: Table S1. Atomic coordinates and equivalent isotropic displacement parameters. Table S2. Bond lengths (Å) for **1**. Table S3. Bond angles (°) for **1**. Table S4. Anisotropic displacement parameters.

Author Contributions: Conceptualization, M.M. and F.M.; investigation, A.T. and G.C.; writing—original draft preparation, M.M. and F.M.; writing—review and editing, M.M., S.V., and F.M.; supervision, S.V. and F.M. All authors have read and agreed to the published version of the manuscript.

Funding: This work was funded by the University of Milan, "Linea B".

Data Availability Statement: Crystallographic data (CCDC entry: 2213557) can be obtained free of charge via www.ccdc.cam.ac.uk/conts/retrieving.html (or from the Cambridge Crystallographic Data Centre, 12, Union Road, Cambridge CB21EZ, UK; fax: ++44 1223 336 033; or deposit@ccdc.cam.ac.uk).

Conflicts of Interest: The authors declare no conflict of interest.

References

1. World Health Organization. *Global Tuberculosis Report 2021*; WHO: Geneva, Switzerland, 2021; ISBN 9789240037021.
2. Chiarelli, L.R.; Mori, G.; Esposito, M.; Orena, B.S.; Pasca, M.R. New and Old Hot Drug Targets in Tuberculosis. *Curr. Med. Chem.* **2016**, *23*, 3813–3846. [CrossRef]
3. Cazzaniga, G.; Mori, M.; Chiarelli, L.R.; Gelain, A.; Meneghetti, F.; Villa, S. Natural products against key Mycobacterium tuberculosis enzymatic targets: Emerging opportunities for drug discovery. *Eur. J. Med. Chem.* **2021**, *224*, 113732. [CrossRef] [PubMed]
4. Ejalonibu, M.A.; Ogundare, S.A.; Elrashedy, A.A.; Ejalonibu, M.A.; Lawal, M.M.; Mhlongo, N.N.; Kumalo, H.M. Drug Discovery for Mycobacterium tuberculosis Using Structure-Based Computer-Aided Drug Design Approach. *Int. J. Mol. Sci.* **2021**, *22*, 13259. [CrossRef] [PubMed]
5. Motamen, S.; Quinn, R.J. Analysis of Approaches to Anti-tuberculosis Compounds. *ACS Omega* **2020**, *5*, 28529–28540. [CrossRef] [PubMed]
6. Buroni, S.; Chiarelli, L.R. Antivirulence compounds: A future direction to overcome antibiotic resistance? *Future Microbiol.* **2020**, *15*, 299–301. [CrossRef]
7. Chiarelli, L.R.; Mori, M.; Barlocco, D.; Beretta, G.; Gelain, A.; Pini, E.; Porcino, M.; Mori, G.; Stelitano, G.; Costantino, L.; et al. Discovery and Development of Novel Salicylate Synthase (MbtI) Furanic Inhibitors as Antitubercular Agents. *Eur. J. Med. Chem.* **2018**, *155*, 754–763. [CrossRef]
8. Chao, A.; Sieminski, P.J.; Owens, C.P.; Goulding, C.W. Iron Acquisition in *Mycobacterium tuberculosis*. *Chem. Rev.* **2019**, *119*, 1193–1220. [CrossRef]
9. Shyam, M.; Shilkar, D.; Rakshit, G.; Jayaprakash, V. Approaches for targeting the mycobactin biosynthesis pathway for novel anti-tubercular drug discovery: Where we stand. *Expert Opin. Drug Discov.* **2022**, *17*, 699–715. [CrossRef]
10. Chiarelli, L.R.; Mori, M.; Beretta, G.; Gelain, A.; Pini, E.; Sammartino, J.C.; Stelitano, G.; Barlocco, D.; Costantino, L.; Lapillo, M.; et al. New Insight into Structure-Activity of Furan-based Salicylate Synthase (MbtI) Inhibitors as Potential Antitubercular Agents. *J. Enzyme Inhib. Med. Chem.* **2019**, *34*, 823–828. [CrossRef]
11. Mori, M.; Stelitano, G.; Gelain, A.; Pini, E.; Chiarelli, L.R.; Sammartino, J.C.; Poli, G.; Tuccinardi, T.; Beretta, G.; Porta, A.; et al. Shedding X-ray Light on the Role of Magnesium in the Activity of M. tuberculosis Salicylate Synthase (MbtI) for Drug Design. *J. Med. Chem.* **2020**, *63*, 7066–7080. [CrossRef]
12. Mori, M.; Stelitano, G.; Chiarelli, L.R.; Cazzaniga, G.; Gelain, A.; Barlocco, D.; Pini, E.; Meneghetti, F.; Villa, S. Synthesis, Characterization, and Biological Evaluation of New Derivatives Targeting MbtI as Antitubercular Agents. *Pharmaceuticals* **2021**, *14*, 155. [CrossRef] [PubMed]
13. Mori, M.; Stelitano, G.; Griego, A.; Chiarelli, L.R.; Cazzaniga, G.; Gelain, A.; Pini, E.; Camera, M.; Canzano, P.; Fumagalli, A.; et al. Synthesis and Assessment of the In Vitro and Ex Vivo Activity of Salicylate Synthase (Mbti) Inhibitors as New Candidates for the Treatment of Mycobacterial Infections. *Pharmaceuticals* **2022**, *15*, 992. [CrossRef] [PubMed]
14. Farrugia, L.J. WinGX and ORTEP for Windows: An update. *J. Appl. Crystallogr.* **2012**, *45*, 849–854. [CrossRef]
15. Singla, L.; Yadav, H.R.; Choudhury, A.R. Evaluation of fluorine-mediated intermolecular interactions in tetrafluorinated tetrahydro-iso-quinoline derivatives: Synthesis and computational studies. *Acta Crystallogr. Sect. B Struct. Sci. Cryst. Eng. Mater.* **2020**, *76*, 604–617. [CrossRef] [PubMed]
16. Urner, L.M.; Young Lee, G.; Treacy, J.W.; Turlik, A.; Khan, S.I.; Houk, K.N.; Jung, M.E. Intramolecular N−H···F Hydrogen Bonding Interaction in a Series of 4-Anilino-5-Fluoroquinazolines: Experimental and Theoretical Characterization of Electronic and Conformational Effects. *Chem.—Eur. J.* **2022**, *28*, e202103135. [CrossRef]
17. Cazzaniga, G.; Mori, M.; Meneghetti, F.; Chiarelli, L.R.; Stelitano, G.; Caligiuri, I.; Rizzolio, F.; Ciceri, S.; Poli, G.; Staver, D.; et al. Virtual screening and crystallographic studies reveal an unexpected γ-lactone derivative active against MptpB as a potential antitubercular agent. *Eur. J. Med. Chem.* **2022**, *234*, 114235. [CrossRef] [PubMed]
18. Jelsch, C.; Ejsmont, K.; Huder, L. The enrichment ratio of atomic contacts in crystals, an indicator derived from the Hirshfeld surface analysis. *IUCrJ* **2014**, *1*, 119–128. [CrossRef]
19. Jiang, S.; He, M.; Xiang, X.W.; Adnan, M.; Cui, Z.N. Novel S-Thiazol-2-yl-furan-2-carbothioate Derivatives as Potential T3SS Inhibitors against Xanthomonas oryzae on Rice. *J. Agric. Food Chem.* **2019**, *67*, 11867–11876. [CrossRef]
20. Chen, J.; Reibenspies, J.; Derecskei-Kovacs, A.; Burgess, K. Through-space 13 C– 19 F coupling can reveal conformations of modified BODIPY dyes. *Chem. Commun.* **1999**, 2501–2502. [CrossRef]
21. Stewart, J.J.P. *MOPAC2016*; Stewart Computational Chemistry: Colorado Springs, CO, USA, 2016.
22. Burla, M.C.; Caliandro, R.; Carrozzini, B.; Cascarano, G.L.; Cuocci, C.; Giacovazzo, C.; Mallamo, M.; Mazzone, A.; Polidori, G. Crystal structure determination and refinement via SIR2014. *J. Appl. Crystallogr.* **2015**, *48*, 306–309. [CrossRef]

23. Sheldrick, G.M. Crystal structure refinement with SHELXL. *Acta Crystallogr. Sect. C Struct. Chem.* **2015**, *71*, 3–8. [CrossRef] [PubMed]
24. Nardelli, M. PARST 95—An update to PARST: A system of Fortran routines for calculating molecular structure parameters from the results of crystal structure analyses. *J. Appl. Crystallogr.* **1995**, *28*, 659. [CrossRef]
25. Bruno, I.J.; Cole, J.C.; Kessler, M.; Luo, J.; Motherwell, W.D.S.; Purkis, L.H.; Smith, B.R.; Taylor, R.; Cooper, R.I.; Harris, S.E.; et al. Retrieval of Crystallographically-Derived Molecular Geometry Information. *J. Chem. Inf. Comput. Sci.* **2004**, *44*, 2133–2144. [CrossRef] [PubMed]
26. MacRae, C.F.; Sovago, I.; Cottrell, S.J.; Galek, P.T.A.; McCabe, P.; Pidcock, E.; Platings, M.; Shields, G.P.; Stevens, J.S.; Towler, M.; et al. Mercury 4.0: From visualization to analysis, design and prediction. *J. Appl. Crystallogr.* **2020**, *53*, 226–235. [CrossRef]
27. Spackman, P.R.; Turner, M.J.; McKinnon, J.J.; Wolff, S.K.; Grimwood, D.J.; Jayatilaka, D.; Spackman, M.A. CrystalExplorer: A program for Hirshfeld surface analysis, visualization and quantitative analysis of molecular crystals. *J. Appl. Crystallogr.* **2021**, *54*, 1006–1011. [CrossRef]